Folding of mRNA-DNA Origami for Controlled Translation and Viral Vector Packaging

Seitz, Iris

Wiley Blackwell
2025-02-27

Seitz, I, Saarinen, S, Wierzchowiecka, J, Kumpula, E-P, Shen, B, Cornelissen, J J L M, Linko, V, Huiskonen, J T & Kostiainen, M A 2025, 'Folding of mRNA-DNA Origami for Controlled Translation and Viral Vector Packaging', Advanced Materials, vol. 37, no. 15, 2417642. https://doi.org/10.1002/adma.202417642

http://hdl.handle.net/10138/598342
10.1002/adma.202417642

ADVANCED MATERIALS
www.advmat.de

Folding of mRNA-DNA Origami for Controlled Translation and Viral Vector Packaging

*Iris Seitz, Sharon Saarinen, Julia Wierzchowiecka, Esa-Pekka Kumpula, Boxuan Shen, Jeroen J. L. M. Cornelissen, Veikko Linko, Juha T. Huiskonen, and Mauri A. Kostiainen**

mRNA is an important molecule in vaccine development and treatment of genetic disorders. Its capability to hybridize with DNA oligonucleotides in a programmable manner facilitates the formation of RNA-DNA origami structures, which can possess a well-defined morphology and serve as rigid supports for mRNA delivery. However, to date, comprehensive studies on the requirements for efficient folding of mRNA into distinct mRNA-DNA structures while preserving its translation functionality remain elusive. Here, the impact of design parameters on the folding of protein-encoding mRNA into mRNA-DNA origami structures is systematically investigated and the importance of the availability of ribosome-binding sequences on the translation efficiency is demonstrated. Furthermore, these hybrid structures are encapsulated inside virus capsids resulting in protecting them against nuclease degradation and also in enhancement of their cellular uptake. This multicomponent system therefore showcases a modular and versatile nanocarrier. The work provides valuable insight into the design of mRNA-DNA origami structures contributing to the development of mRNA-based gene delivery platforms.

1. Introduction

Nucleic acids play a key role as therapeutic agents by directly targeting genes and subsequently modulating their expression.[1] Therefore, they find versatile applications in protein replacement therapy,[2] gene silencing,[3] and as vaccines.[4,5] Nucleic acid therapeutics are highly specific,[1] however, their success is dependent on the (intra)cellular delivery, which can be enhanced by complexing the nucleic acids into nanoscale particles. The transfection efficiency is furthermore influenced by the size, shape, and the surface chemistry of the nanoparticle.[6,7] Subsequently, packaging of high molecular weight nucleic acids, including gene-encoding nucleic acids and mRNAs, into a compact, predefined shape would be desirable. However, this remains challenging using conventional agents such as lipids.[8]

An attractive alternative for the development of a multicomponent delivery platform is offered by utilizing the DNA origami technique.[9] It allows the fabrication of predefined, custom-shaped 2D and 3D DNA nanostructures[10,11] by folding a long, single-stranded DNA (ssDNA) scaffold into a desired shape with the help of "stapling" DNA oligonucleotides.[9,12] DNA origami structures are highly addressable, allowing for site-specific functionalization[13] with targeting agents like antibodies, affibodies, aptamers and peptides for improved drug delivery.[14,15] The choice of scaffold strand is no longer limited to generic, bacteriophage-genome-derived sequences,[16] as the fabrication schemes based on synthetic, gene-encoding scaffolds have become available.[17,18] Similarly, the DNA scaffold can be replaced with mRNA, which facilitates protein translation without the need to enter the nucleus.[19] The mRNA can be folded into the predefined shape[20] using either kissing loops following the RNA origami technique[21–23] or ssDNA staple strands, resulting in a mRNA-DNA structure, serving as the "core" of such a

I. Seitz, S. Saarinen, J. Wierzchowiecka, V. Linko, M. A. Kostiainen
Department of Bioproducts and Biosystems
Aalto University
00076 Aalto, Finland
E-mail: mauri.kostiainen@aalto.fi

E.-P. Kumpula, J. T. Huiskonen
Institute of Biotechnology, Helsinki Institute of Life Science HiLIFE
University of Helsinki
00014 Helsinki, Finland

The ORCID identification number(s) for the author(s) of this article can be found under https://doi.org/10.1002/adma.202417642

DOI: 10.1002/adma.202417642

B. Shen
Department of Medical Biochemistry and Biophysics
Karolinska Institutet
17177 Stockholm, Sweden

J. J. L. M. Cornelissen
Department of Molecules and Materials, MESA+ Institute for Nanotechnology
University of Twente
7522 Enschede, The Netherlands

V. Linko
Institute of Technology
University of Tartu
50411 Tartu, Estonia

M. A. Kostiainen
LIBER Center of Excellence
Aalto University
00076 Aalto, Finland

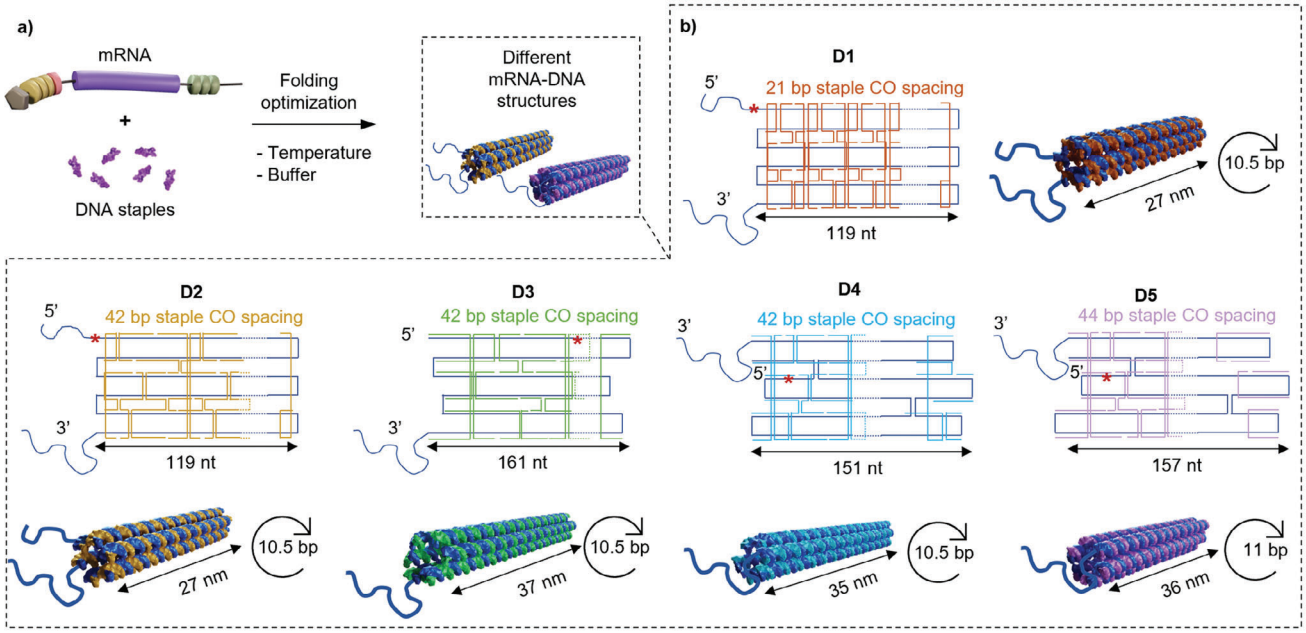

Figure 1. a) A 996-nt mRNA including an EGFP-encoding sequence is hybridized with short ssDNA strands by thermal annealing resulting in mRNA-DNA origami variants which differ in their internal design. The folding conditions with regard to buffer composition and annealing temperature are optimized for every design. b) The designs (D1–D5) differ in the scaffold routing with respect to the scaffold crossovers (CO) and embedment of the 5'-cap region (the start codon is marked with an asterisk), the staple CO spacing (orange, yellow, green, light blue, light purple), and the helical rise of the mRNA-DNA duplex, given as bp per turn.

multicomponent system. Recently, several RNA-DNA origami structures have been presented, aiming to mediate the delivery of both mRNA and antisense oligonucleotides.[24–27]

The design of (multilayer) DNA origami structures is commonly based on a square or a honeycomb lattice, resembling the canonical *B*-form of duplex DNA with 10.67 or 10.5 base pairs (bp) per helical turn, respectively.[28] In contrast, in RNA origami, the double-helical RNA domains adopt the *A*-form, resulting in 11 bp per turn.[22] Previously reported RNA-DNA origami were designed to have either 10.5, 10.67, or 11 bp per turn.[24,26,29] Although a tendency toward the *A*-form, i.e., 11 bp per turn has been suggested for short RNA-DNA structures,[30] a thorough study on the design parameters for folding and subsequent translation has not yet been realized.

In this article, we explore the design of a six-helix bundle (6HB) mRNA-DNA origami with respect to its folding and translation properties. To this end, a protein-encoding mRNA scaffold is folded into distinct nanostructures using short ssDNA staples (**Figure 1**a). Thus, certain parts of the mRNA, for instance the poly(A)-tail, can be purposely left non-hybridized. First, we investigate the impact of the internal design, i.e.,, the crossover (CO) spacing and the number of bp per helical turn, on the folding efficiency, while also changing the buffer environment and temperature gradient of the folding reaction (Figure 1a,b). By additionally adjusting the single-stranded parts in the mRNA-DNA origami, we ensure the preservation of the innate translation property of mRNA once it is folded. In a second step, we use virus capsid proteins to encapsulate the mRNA-DNA origami, resulting in a structurally well-defined protein-based nanocarrier. The protein capsid is not only found to improve protection of the nucleic acid structure against nuclease degradation, but it also enhances the nanocarrier's uptake into cells and henceforth allows the mRNA's translation into the target protein while exhibiting minimal toxicity in the system studied.

2. Results

2.1. Design Rationale for mRNA-DNA Origami

We designed five different honeycomb lattice -based 6HB mRNA-DNA origami variants (Figure 1b) to investigate possible structural limitations during the folding process as well as their properties regarding stability and translation efficiency. To facilitate the translation characterization, we selected a 996-nucleotide (nt) long mRNA, which includes an enhanced green fluorescent protein (EGFP) encoding sequence, as our scaffold (blue).

For folding the mRNA scaffold with DNA staple strands, we started off with two variants, where only the mRNA's EGFP encoding part (714 nt) was hybridized, i.e., the poly(A)-tail and the 5'-cap region of the mRNA, in which the start codon (AUG) is positioned, remained non-hybridized, thus resulting in 27-nm long structures. These variants additionally featured 7–8-nt long scaffold loops, i.e., single-stranded regions of the scaffold at the both ends. Since the spacing of inter-helical staple COs between neighboring helices was previously found to affect the stability of 6HB DNA origami structures,[31] two different CO spacings were tested: the COs were spaced either at 21 bp (Figure 1b, D1, orange, top right) or 42 bp intervals (D2, yellow, bottom left) (i.e., 21 or 42 bp between COs that link the same neighboring helices).

Keeping the CO spacing at 42 bp, a 37-nm long version without the scaffold loops was designed, in which the 5'-cap region was hybridized with the staples (D3, green, bottom middle-left).

To further increase the stability and rigidity, scaffold COs were included in the structures to obtain a structure with 35 nm in length (D4, light blue, bottom middle-right).

The helical rise of the variants D1–4 was set to 10.5 bp per turn, thus resembling *B*-DNA and being in line with previously reported RNA-DNA origami.[24,26] To decrease strain in the origami structure, complying with the tendency of short RNA-DNA duplexes toward the *A*-DNA geometry,[30] the design of the fifth variant (36 nm in length) also featured two scaffold COs and the hybridization of the 5'-cap region, but its helical pitch was set to 11 bp per turn (D5, light purple, bottom right).

In addition, all design variants included four staples that could be replaced with extended staples to further facilitate attachment of ATTO590 dye (A590) -modified DNA stands through DNA-DNA hybridization. It allows tracking of the origami, in addition to ethidiumbromide (EtBr), under red light (Alexa A647 channel for gels and AF594 channel for uptake into cells).

2.2. Optimization of the Folding Environment for mRNA-DNA Origami

The folding of DNA origami structures is usually performed in a buffered one-pot reaction by first heating the solution and then gradually cooling it to room temperature. The optimal buffer composition (folding buffer; FOB), including mainly divalent cations to screen the negative charges of the nucleic acid backbones as well as the temperature gradient are both structure specific.[28] In comparison to DNA, RNA is more susceptible to chemical degradation due to the presence of a 2'-hydroxyl group[32] which can interact with a phosphate group resulting in transesterification.[33] This degradation reaction is influenced by the pH of the buffer,[32] concentration of divalent cations as well as the temperature,[32,33] making a screening of both ion concentration and temperature essential. To this end, we started off by applying previously reported RNA-DNA origami folding conditions to our designs, which allows us to focus on the ion screening. Initially, a Tris-ethylenediaminetetraacetic acid (EDTA) -based buffer (TE) supplemented with 0–100 mM NaCl was chosen for folding the mRNA-DNA origami. The reaction mixture was cooled down overnight from 65 to 20 °C (**Figure 2a–d**, top panel; Note S1, Supporting Information).

The outcome of the folding reactions was monitored using agarose gel electrophoresis (AGE), transmission electron microscopy (TEM), and atomic force microscopy (AFM). Note, that the characterization was performed before purification of excess staple strands. Both D1 (Figure S1a, Supporting Information) and D2 (Figure 2a, top panel) showed a very similar electrophoretic mobility compared to the mRNA scaffold for all NaCl concentrations tested. At high salt concentrations a decrease in the intensity and broadening of the leading band was observed. However, the folding efficiency was low, since mainly unfolded or aggregated mRNA were observed under TEM (30 mM NaCl; Figure 2a; Figure S2a, Supporting Information) and the few folded structures were shorter than expected (≈21 nm).

Similar results were also obtained for D3 and D4. While D3 and D4 (Figure 2b,c, top panel) showed reduced mobility compared to the plain mRNA scaffold, also an additional, even slower migrating band appeared. The number of correctly folded structures observed in TEM was low for both D3 and D4 (30 mM NaCl; Figure 2b,c; Figure S2b,c, Supporting Information) as the lengths of the folded objects appeared to be only ≈16–29 nm (D3) and 20–29 nm (D4). The low yield and observation of only truncated structures for D2–D4 suggests a potential kinetic trap during the origami folding process.

By increasing the helical pitch from 10.5 bp per turn to 11 bp per turn in D5, two bands with decreased mobilities were observed (Figure 2d, top panel). In comparison to D4, it was noticeable that the leading band vanished gradually at higher NaCl concentration. When folded with a buffer supplemented with 30 mM NaCl, a higher number of folded structures compared to D4 was observed, however, the large spread in the size distribution remained, with the majority of the structures having lengths between 16–26 nm, suggesting the presence of partially folded structures (Figure S3a, Supporting Information). An increase of NaCl to 100 mM resulted in an overall increase in the length of the observed folding products, displaying also a low number of structures with the designed, theoretical dimensions of D5 (Figure 2d; Figure S3b, Supporting Information).

In general, Mg^{2+} cations are considered preferential for the folding and stabilization of complex RNA structures compared to Na^+,[34,35] however, they also promote the chemical degradation of the RNA. This both protective and degradative behavior of the Mg^{2+} cations is highly concentration dependent,[36] and can be further influenced by chelating agents like EDTA.[37,38] Aiming to further increase the yield of the folding reactions for all structure variants, the buffer composition was altered to a Tris-acetate-EDTA (TAE) buffer supplemented with $MgCl_2$ (Figure 2a–d, bottom panel). Simultaneously, the folding temperature was set to 55 °C and the folding was performed isothermally for 15 min, after which the samples were place on ice for 10 min. While degradation of the mRNA could not be detected using electrophoresis (Figure S4, Supporting Information), these changes in the folding conditions resulted in better folding outcomes for all our designs. The shift in electrophoretic mobility compared to plain mRNA was still minimal for D1 (Figure S1b,c, Supporting Information) and D2 (Figure 2a, bottom panel), but TEM and AFM showed correctly folded D2 variants (Figure 2a, bottom panel; Figure S5a, Supporting Information). The observed D2 dimensions (given as average (avg) ± s.d. throughout) both in length (l) with $l_{avg} = 29.8 \pm 3.8$ nm and diameter (d) with $d_{avg} = 6.5 \pm 1.0$ nm correspond well with the designed ones.

For both D3 and D4 (Figure 2b,c, bottom panel; and Figure S5b,c, Supporting Information, respectively) full length structures could be observed, however, the scattering in the length distribution persisted also in these conditions, resulting in $l_{avg} = 30.7 \pm 8.0$ nm for D3 and $l_{avg} = 26.4 \pm 8.3$ nm for D4.

Analysis of the folding reaction of D5 on an agarose gel (Figure 2d, bottom) revealed a leading band, which migrated slower than the plain mRNA, and an additional band, suggesting the formation of dimers. Indeed, both monomers ($l_{avg} = 40.1 \pm 3.4$ nm, $d_{avg} = 5.9 \pm 0.9$ nm) and dimers ($l_{avg} = 76.0 \pm 10.5$ nm, $d_{avg} = 6.4 \pm 0.8$ nm) were observed under TEM (Figure S5d, Supporting Information), and their dimensions were in good agreement with the theoretical ones.

Alternatively, K^+ cations can stabilize the tertiary structure of RNA[35] and their usage has been reported for a wireframe RNA-DNA origami structure, supplementing 10 mM HEPES

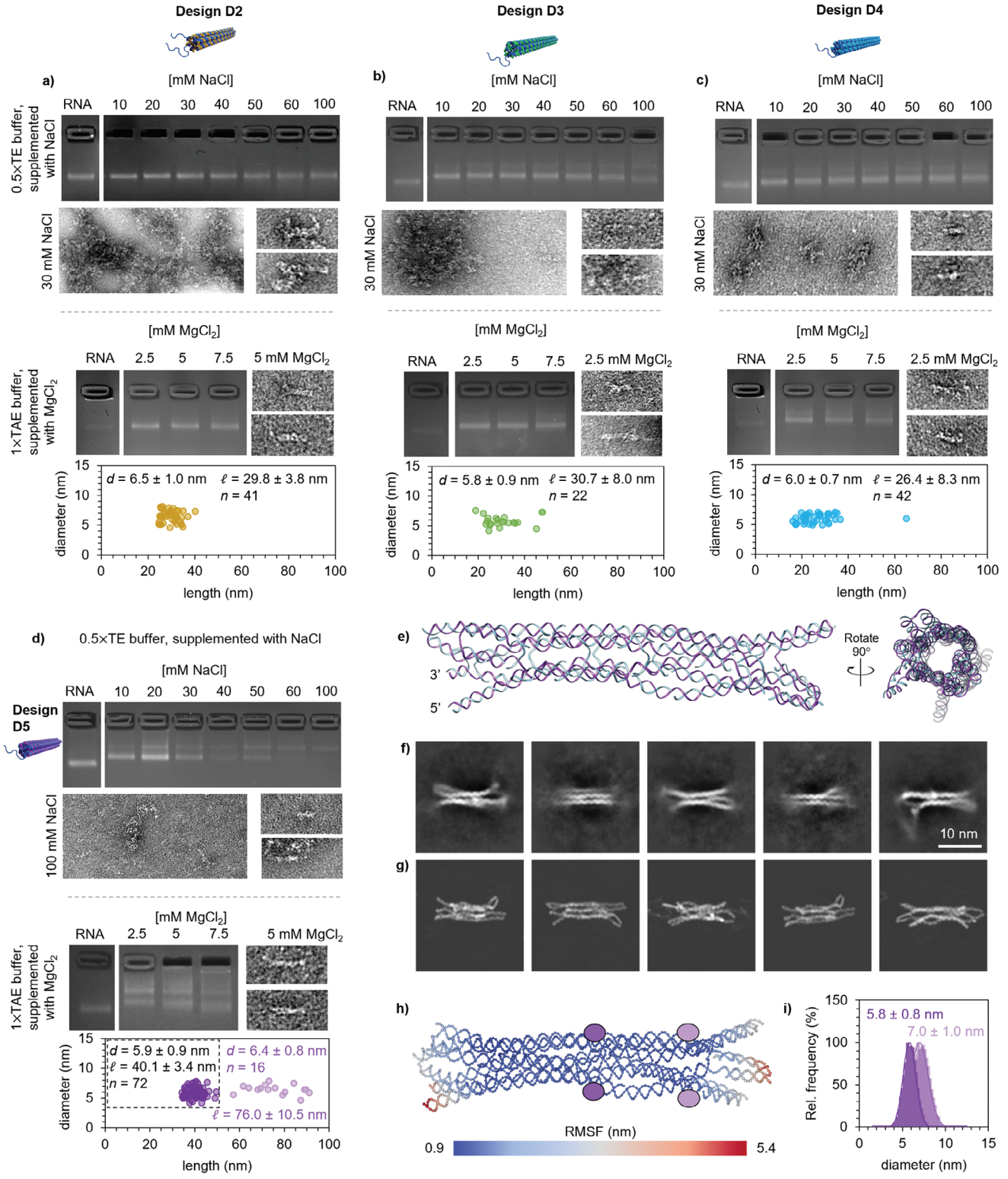

(4-(2-hydroxyethyl)-piperazine-1-ethane-sulfonic acid) buffers[27] (Note S2, Supporting Information). Even though folding was observed for design variants D2–D5, it was most pronounced for D5, being in line with results obtained from Tris-based buffers. The folding temperature was found to substantially effect the yield, most likely due to chemical degradation of the mRNA template during the folding process at high temperatures.[33] Since divalent cations are commonly used for the folding of DNA origami, and since Mg^{2+} cations have been reported beneficial for the folding and stabilization of tertiary RNA structures,[35,36] we decided to proceed with TAE/Mg^{2+}-buffers in combination with short, isothermal folding.

Despite the observation of full length structures for all mRNA-DNA origami variants folded in those conditions, the folding yields were found to differ between the designs. To further quantify the success of the folding reaction, the structures were folded in their optimized conditions, i.e., 1× TAE supplemented with 5 mM $MgCl_2$ for D1, D2 and D5, and 2.5 mM $MgCl_2$ for D3 and D4, and subsequently, they were subjected to treatment with RNase A (0–10 U mL^{-1}, Note S3, Supporting Information), since it can digest ssRNA[39] at high salt concentrations. All folded variants except D1 elicited an increased resistance, with D5 performing the best.

Overall, the differences in the observed folding yields for origami variants can be attributed to the internal design. D2 has no scaffold COs, and the staple CO spacing of 42 bp makes the structure rather flexible allowing for mechanically less restrained folding and also high yields. In comparison, an increase of the CO spacing in D1 (21 bp intervals) seems to hamper its folding, since almost no folded structures could be observed.

Despite having a staple CO spacing of 42 bp in D3, it differs from D2 in the scaffold routing, including the removal of scaffold loops and hybridization of the 5'-cap region, alterations which seem to decrease the folding yield. The addition of two scaffold crossovers in the scaffold routing of D4, in combination with the mismatch in the helical pitch between the mRNA scaffold and the DNA staples most likely reduced the degree of freedom for the staple strands to bind correctly, thus resulting in a further decrease of the folding yield.

Increasing, in return, the helical pitch from 10.5 to 11 bp per turn in D5 resulted in a high yield of well-folded structures. Since D5 tended to form dimers, the folding conditions were further optimized (Note S4, Supporting Information), leading to a final buffer composition of 1× TAE supplemented with 5 mM $MgCl_2$ and 1 mM NaCl. For a more detailed structural characterization of D5, molecular dynamic simulations (Figure 2e) were carried out using oxDNA.[40,41] D5 was stable over the course of the simulation, and found to have a relatively compact middle part accompanied by more flexible structure ends. Additionally, D5 was analysed using cryogenic electron microscopy (cryo-EM, Figure 2f; Figure S13, Supporting Information). The 2D classification of the picked particles suggested a folded middle part comprised of several helices. The 2D class averages were subsequently projection matched with the oxDNA simulated model (Figure 2g) and found to be in agreement. Owing the high flexibility especially toward the both ends of the mRNA-DNA origami (Figure 2h) caused by a low number of staple crossovers in the corresponding regions, it was not possible to reconstruct an accurate 3D model at high resolution. Nevertheless, the distance between two nucleotides positioned on opposing helices, corresponding to the 6HB diameter, was traced over the course of the simulation (Figure 2i) and found to match the measured diameter obtained from negative-stain TEM (Figure 2d, bottom).

Based on all these observations discussed above, internal design parameters such as a simple scaffold routing without COs, a staple CO spacing of 44 bp and a helical pitch of 11 bp per turn are suggested to enhance the folding yield. Subsequently, we selected variants D2 and D5 folded in TAE/Mg^{2+}-buffers for further studies.

To further demonstrate the applicability of our proposed design parameters, we designed two alternative mRNA-DNA origami 6HB structures (Note S6, Supporting Information) which were based on mRNA sequences that encode either firefly luciferase (mFLuc, 1922 nt) or β-galactosidase (mβ-gal, 3421 nt). Using the optimized folding conditions, these mRNA scaffolds were successfully assembled into elongated structures with the expected dimensions.

2.3. Importance of the Ribosome Binding Site Positioning in Translation

For potential applications, also the disassembly/unfolding of the mRNA-DNA origami and subsequent translation of the mRNA are highly important. Therefore, the translation was first studied in an extracellular environment using reticulocyte lysate (**Figure 3a**). To this end, both D2 and D5 structures were folded using their respective optimized folding conditions in TAE/Mg^{2+}-buffer and subsequently purified from excess staple strands. The outcome of the translation was analyzed by native polyacrylamide gel electrophoresis (PAGE). While D2 was successfully translated into EGFP (Figure 3b,c, first lane, yellow bar), appearing as a fluorescent band upon excitation with blue light (Alexa A488 channel), no signal was obtained for D5 (second lane, light purple bar).

Figure 2. a–d) top, Optimization of the buffer conditions in the folding reaction for each design variant by supplementing 0.5× TE buffer with 0–100 mM NaCl. The success of the folding reaction is evaluated from the change in electrophoretic mobility on a 3.5 % agarose gel. Negative-stain TEM images of unpurified samples display aggregated structures (left; image width corresponds to 325 nm) as well as discrete folded structures (right, image width corresponds to 100 nm). (a–d) bottom, Optimization of the folding conditions using isothermal temperature and screening of the $MgCl_2$ concentration in 1× TAE buffer. Analysis of the optimized conditions by assessing the electrophoretic mobility of the folded structures, negative-stain TEM images (unpurified samples; image width corresponds to 100 nm) of plain mRNA-DNA origami and observed dimensions of the folded structures. For D5, the average dimensions are calculated separately for monomers (dark) and dimers (light). The dimensions are given as avg ± s.d e) Side (left) and top (right) view of the mean structure of D5 obtained from oxDNA simulations. The scaffold is colored in purple, the staple strands in blue. f) Representative 2D class averages of D5 obtained from cryo-EM. g) Projection match between the 2D class averages and the oxDNA simulated model. h) The root mean square fluctuation (RMSF) of each nucleotide displays high flexibility of the helices at the both ends of the 6HB (D5). i) Observed distribution of the diameter of 6HB (D5) at two different positions on the simulated model (marked in h) measured as the distance between two nucleotides on opposing helices.

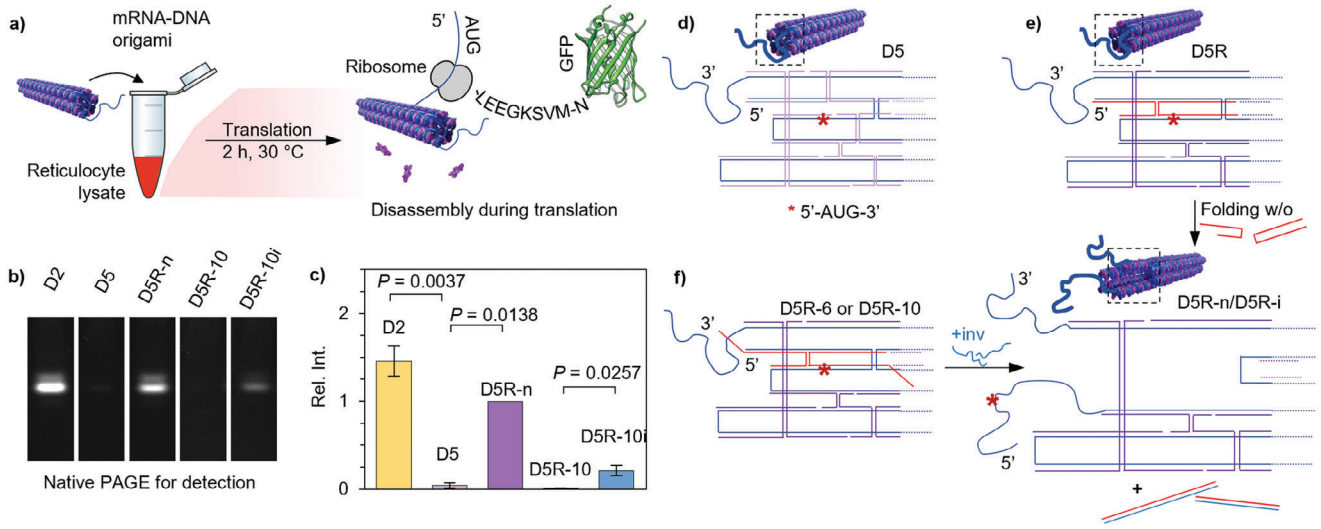

Figure 3. a) Addition of the folded mRNA-DNA origami to reticulocyte lysate results in extracellular translation into EGFP. b) The fluorescence signal is detected using native PAGE. c) Relative intensities of the fluorescence signals obtained from (b). The data is given as avg ± s.d. of $n = 3$ samples. d) Design of the staple strands (light purple) that hybridize with the 5'-cap region of the mRNA for D5, with the position of the start codon in mRNA scaffold (blue) being marked by an asterisk. e) Redesign of the staples leaves only two replacement strands that hybridize with the 5'-cap region of the mRNA (variant D5R, replacement strands marked with red). f) The replacement strands can also be designed with 3'-overhangs (D5R-6 or D5R-10). The addition of invader strands (inv, blue) leads to hybridization with the replacement strand, which subsequently releases the 5'-cap region of the mRNA. The same result can be obtained from (e) by omitting the replacement strands in the folding mixture.

In eukaryotes, the process of ribosome recruitment starts usually at the 5'-cap region of the mRNA. As soon as the start codon is reached, translation is initiated.[42] Apart from the helical geometry, D2 and D5 differ mainly in the configuration of the 5'-cap region. While it is part of the folded core of D5 (Figure 3d, the start codon marked with an asterisk), it is non-hybridized and therefore freely available in D2 (see Figure 1b).

To probe the role of hybridization of the mRNA's 5'-region, the staple design downstream of the 5'-cap of D5 was revised. In the revised version (D5R, purple), the 5'-region of the mRNA was hybridized only with two replacement staple strands (red strands in Figure 3e). Both replacement staple strands were also designed with 3'-overhangs (variant D5R-6 or D5R-10, Figure 3f; Figure S16, Supporting Information), thus facilitating a triggered release of the replacement strands through a toehold-mediated strand displacement reaction using invader strands (inv, blue). Now, by either omitting these two replacement staple strands from the staple mixture or by adding the invader strands, a freed 5'-cap region was obtained (D5R-n or D5R-i), resulting in a structure with four full-length and two truncated helices as depicted in the schematic (Figure 3e,f). Neither the addition of the 3'-overhangs nor the omission of the replacement strands were found to adversely affect the folding (Figure S16e, Supporting Information).

The importance of the accessibility of the 5'-cap region was confirmed by reperforming the translation studies with D5R-n, which revealed successful mRNA translation into EGFP (Figure 3b,c third lane, purple bar). However, in comparison to D2, the protein translation yield was reduced by one third. Additionally, the irreversible unfolding of the 5'-cap region through the strand displacement reaction and the subsequent translation of the mRNA was demonstrated. To this end, the translation of D5R-6 and D5R-10, which featured 6 nt or 10 nt long toeholds on the replacement strands, respectively, was investigated first without the addition of an invader strand. As expected, no translation activity was observed (Figure 3b,c, fourth lane, red bar; Figure S17a, Supporting Information), confirming that the toeholds do not interfere with the origami folding. Subsequently, D5R-6 and D5R-10 were incubated with 10× excess of the corresponding invader strands for 10 min prior to their addition to the reticulocyte lysate. While the signal obtained from D5R-6i was negligible (Figure S17a, Supporting Information), a weak fluorescence band was observed for D5R-10i (Figure 3b,c, fifth lane, blue bar), showing that the toehold-mediated irreversible unfolding of the 5'-cap region allowed to recover 20 % of the fluorescence intensity when compared to D5R-n.

Moreover, the translation capability of the remaining variants was tested similarly. However, due to degradation of D1, D3, and D4 during the removal of excess staples, all mRNA-DNA origami variants were subjected to reticulocyte lysate without purification which additionally allows to rule out false positive signals originating from unfolded mRNA that could have been left in solution after the folding reaction and purification (Figure S17b, Supporting Information). The fluorescence intensities from D2, D5 and D5R-n corresponded to the previously observed results, with D2 showing the highest translation activity while the translation of D5 was prohibited. A fluorescence signal could also be detected for D3, which might have been expected based on the folding evaluation. The majority of the observed D3 variants were truncated under TEM, which indicates that the structures were only partially folded, and thus contained longer segments of free, non-hybridized mRNA than intended by the design. Therefore, it is also possible that the start codon in D3 was exposed. In comparison, the translation of D4 was at the detection limit, suggesting a correctly folded 5'-cap region. Surprisingly, the

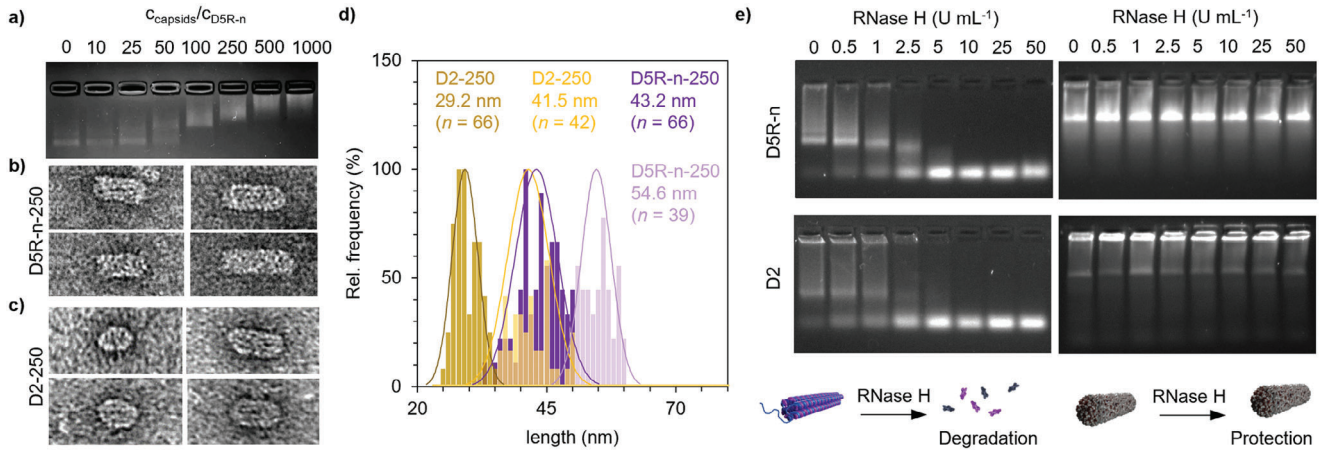

Figure 4. a) The electrophoretic mobility of D5R-n changes with increasing virus capsid protein concentration. b,c) Negative-stain TEM images showing the development of a single protein layer on D5R-n (b) and D2 (c) when using a protein excess of 250. The obtained complexes are grouped based on their lengths; the image width corresponds to 100 nm. d) Observed length distributions (values given correspond to the avg) for D2 and D5R-n -templated complex populations with 250× excess of the virus capsid proteins and the calculated Gaussian distribution (solid line). e) RNase H digestion of plain (left) and complexed (right) D5R-n (top) and D2 (bottom).

EGFP signal obtained for D1 exceeded those of all other variants, suggesting mainly aggregation during the folding reaction, and therefore resulting in easy accessibility of the start codon.

2.4. Protection of mRNA-DNA Origami Using Viral Capsids

Nucleic acids are known for their susceptibility to degradation by nucleases, making their therapeutic use challenging. To maintain the intactness of nucleic acid nanostructures, several strategies have been developed.[14,43] One feasible approach is to create a protective shell around the nucleic acid structures.[44,45] To achieve this, it has been previously demonstrated that capsid proteins isolated from cowpea chlorotic mottle virus (CCMV) can reassemble on DNA origami structures by exploiting electrostatic interactions between the negatively charged origami and the positively charged *N*-terminus of the capsid protein.[46,47]

To assess the complexation between the capsid proteins and the mRNA-DNA origami, D2 and D5R-n were mixed with increasing concentrations of CCMV capsid proteins and the shift in the electrophoretic mobility of the formed complexes was monitored using AGE (**Figure 4a** for D5R-n and Figure S18a for D2). A significant decrease in the mobility was observed for both origami variants already at a protein excess (given as $c_{capsids}/c_{origami}$) of 100, and increasing the protein concentration from that led to further decrease in the mobility.

Aiming to use as low protein concentration as possible for the coating, mRNA-DNA origami complexed with an excess of 250 were selected and imaged with TEM. For both origami variants, the formation of a highly ordered protein coat was observed (Figure 4b,c; Figure S18b,c, Supporting Information). This can be also clearly seen from the increased diameter of the imaged objects: for D5R-n from $d_{avg} = 5.9 \pm 0.9$ nm (plain origami) to $d_{avg} = 18.7 \pm 1.5$ nm (complex) and for D2 from $d_{avg} = 6.5 \pm 1.0$ nm (plain origami) to $d_{avg} = 19.2 \pm 2.0$ nm (complex). The dimensions are in line with previously reported DNA origami-capsid protein complexes.[46]

Interestingly, the coated structures showed a heterogeneity in length, which could be grouped into two main populations (Figure 4d). The first population is formed when the proteins coat the folded core of the structure resulting in complexes with lengths of $l_{avg} = 29.2 \pm 2.5$ nm (D2, dark yellow) and $l_{avg} = 43.2 \pm 4.1$ nm (D5R-n, dark purple). The second population consists of complexes with $l_{avg} = 41.5 \pm 4.0$ nm (D2, light yellow) and $l_{avg} = 54.6 \pm 2.9$ nm (D5R-n, light purple), respectively, suggesting that the free 5'-cap region together with the poly(A)-tail can further template the capsid protein shell formation (Figure S18d, Supporting Information).

To test the possible protection of the coating, both the uncoated and complexed structures were incubated with RNase H (0–50 U mL^{-1}) (Figure 4e), which is known to attack RNA in RNA-DNA complexes.[48] The protein shell was found to enhance the stability of both D5R-n (top) and D2 (bottom) when treated with RNase H, making it possible for the complexed structures to withstand nuclease concentrations up to 50 U mL^{-1} (right gels). The uncoated, plain variants started to degrade already at 0.5 U mL^{-1}, and only subtle differences in the stability and digestion profiles between the variants were observed (Figure 4e, left gels).

In addition, the susceptibility of the structures toward DNase I was studied (Figure S19, Supporting Information). DNase I is known to act non-specifically on ssDNA and the minor groove of double-stranded DNA (dsDNA) by cleaving the phosphodiester bonds.[49] Despite its preference for dsDNA, the enzyme may also show some residual activity toward RNA-DNA duplexes.[49] Throughout the tested DNase I concentration range (0–50 U mL^{-1}), the electrophoretic mobility of D5R-n remained constant, suggesting that D5R-n can withstand the enzyme treatment. For D2, in contrast, an increase in smear was observed once it was treated with 0.5 U mL^{-1} DNase I, most likely originating from the degradation of the DNA staples.

Since both variants were equipped with A590-modified DNA strands through hybridization to complementary DNA staple overhangs (i.e., DNA-DNA duplex formation), the digestion

processes could additionally be monitored in the fluorophore channel (Figure S19, Supporting Information, Alexa647, A647). For both variants, a release of the fluorophores was detected once DNase I was added. However, the leading band of D5R-n could be observed over a wider concentration range in the A647 channel, suggesting a slower degradation of the fluorophore-containing strands. Nevertheless, the virus capsid coating efficiently protected the whole origami from degradation with up to 50 U mL^{-1}.

2.5. Transfection and Translation in Mammalian Cells

Having ensured the accessibility of the 5'-cap region of the mRNA for translation and established a protein shell to prevent degradation by nucleases, the uptake efficiency of the mRNA-DNA origami was tested using HeLa cells (**Figure 5**; Figures S20–S23, Supporting Information). Briefly, the cells were seeded into a 96-well plate and grown for 24 h. Subsequently, the media was exchanged to Opti-MEM, and the cells were incubated with the samples for 16 or 24 h. We used A590 to track the uptake of D2 and D5R-n into the cells, and the signal read-out was performed in 1× PBS using a microplate reader (excitation/emission of 490/520 nm for EGFP and 584/616 nm for A590) and fluorescence microscopy (GFP filter at 470 nm for EGFP and AF594 filter at 590 nm for A590).

We started out with investigating the transfection efficiency of naked structures (N) and structures complexed with virus capsid proteins (C, protein excess of 250) (Figure 5a, top). In addition, these samples were compared to a control sample with the commercially available transfection agent Lipofectamine 2000 (LP2000, Note S12, Supporting Information). While the uptake of both naked (N) and LP2000 treated (L) structures (Figure 5a, top) was found to be low, the A590 signal increased drastically once the viral capsid coating was applied onto the structures (C). This trend was observed for both 16 and 24 h sample incubation with the cells, however, a slightly higher fluorescence signal was obtained after 24 h. Moreover, a sequential combination of virus capsids and LP2000 was tested (C+L), in which mRNA-DNA origami was first complexed with the capsid proteins, followed by the addition of the LP2000 (Figure S24d, Supporting Information). Interestingly, the uptake of such complexes was comparable to the C-samples, suggesting the virus capsid proteins being the driving force in the enhanced uptake. Notably, a significantly higher transfection efficiency was found for D5R-n C+L-samples for both 16 and 24 h in comparison to D2.

Despite the high internalization of the capsid-coated mRNA-DNA origami (C and C+L), the EGFP signal (Figure 5a, bottom) from the C-samples was similar as for the naked structures, suggesting the inaccessibility of the mRNA for the ribosomes. In comparison, L-samples were found to elicit a similar level of translation. Only in the presence of both virus capsid proteins and LP2000 (C+L), a significant change in the EGFP signal was observed, being more pronounced after 24 h. Moreover, it was noted that the average EGFP intensity for D2 was higher than for D5R-n (Figure 5a bottom, b,c), but it was also expected based on the observation during the extracellular transcription. As a control, plain mRNA was subjected to transfection (Note S13, Supporting Information) using the same conditions, which showed higher EGFP intensities. Here, the EGFP signal for L-samples was found to be the highest for short transfection periods with a tendency to decrease over time. In contrast, mRNA C+L-samples showed the opposite trend, with the EGFP signal increasing over time, indicating that the process of both decomplexing the mRNA-DNA origami-based nanocarrier and the unfolding of the mRNA-DNA origami core are relatively slow.

To further investigate the synergistic effect of the C+L coating on both uptake and translation of the mRNA-DNA origami structures, we explored their cellular uptake route (Figure 5d–f; Figures S27 and 28, Supporting Information). Nanoparticles can utilize different pathways for their uptake, which can be blocked by certain, well-studied inhibitors.[50] While sucrose is considered a general inhibitor, cytochalasin D inhibits phagocytosis and macropinocytosis. Dynasore blocks both caveolin- and clathrin-dependent endocytosis, whereas chlorpromazine specifically acts on clathrin-dependent, and filipin III and nystatin on caveolin-dependent endocytosis.

As expected, sucrose was found to decrease the uptake of both D2 (Figure 5d,f) and D5R-n (Figure 5e), regardless of the composition of the coating. More importantly, a similar behaviour was observed for cells treated with dynasore which inhibited the uptake significantly, suggesting mainly caveolin- and clathrin-dependent endocytosis. Notably, the uptake inhibition of C- and C+L-samples was more efficient than that of the L-samples, which was more pronounced for the D5R-n variant. In addition, cytochalasin D and chlorpromazine (for L only) contributed significantly to the uptake inhibition of D5R-n samples, as well as, though to a lesser extent, filipin III and nystatin.

Finally, the toxicity of the samples toward the cells was evaluated (Note S15, Supporting Information). While the cell viability decreased by ≈50 % upon treatment with L-samples, naked structures and samples coated with the virus capsids (C) or with the combination of C+L were not cytotoxic within the studied application relevant concentration range.

2.6. Discussion

We have investigated the folding behavior of a short, 6HB mRNA-DNA origami structure with respect to preserving the mRNA's innate functionality, i.e., its ability to be translated into a protein. To this end, we initially drafted five origami variants, which differed in their internal design. Commonly, the folding of DNA origami is considered to depend on the structure's geometry, and the staple design.[51] Furthermore, the scaffold routing is found to influence the way staples are integrated into the scaffold: the integration may happen either through the initial binding followed by a collapse event or in a uniform manner.[52]

Here, the mRNA-DNA origami variants D1–D3 featured a simple scaffold routing in which neighboring helices are connected at their ends. In contrast, D4–D5 included two scaffold crossovers shifted toward the center, which could be considered as a "forth and back" routed design. Assuming that DNA origami folding pathways apply also to (m)RNA-DNA origami, and taking into account the mismatch between the preferred helical pitches of RNA and DNA duplexes, the scaffold routings of D1–D3 might be more suitable for structures adopting 10.5 bp per helical turn. Since the collapse event is global, small structural mismatches might be easier to accommodate, as opposed to the uniform

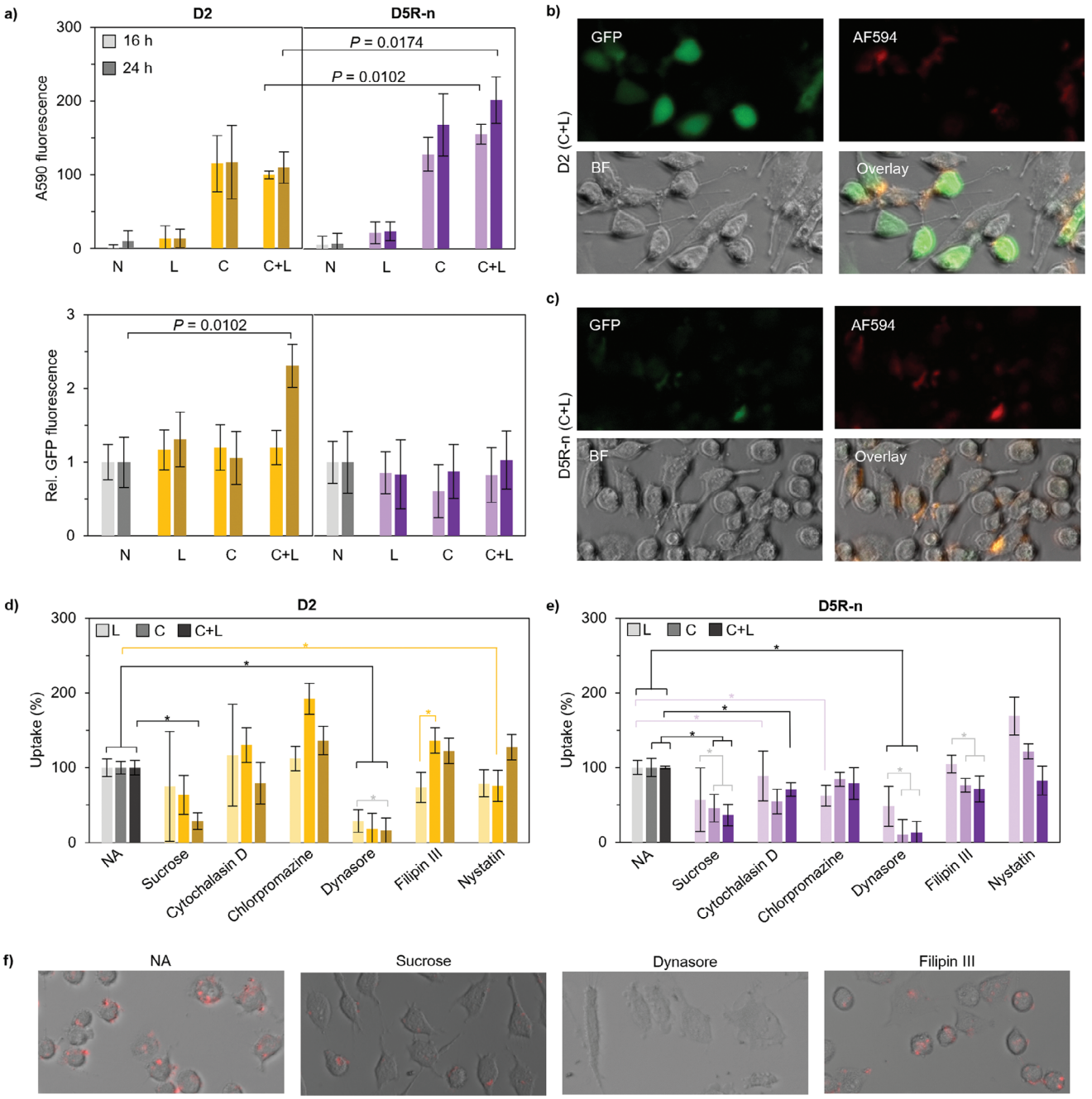

Figure 5. a) Monitoring the uptake of naked (N) and D2 (yellow) and D5R-n (purple) complexed with either LP2000 (L), CCMV capsid proteins (C) or a combination of capsid proteins and LP2000 (C+L) into HeLa cells (top) and the translation activity of the same samples (bottom) for 16 h (light) and 24 h (dark). The data is given as avg ± s.d. of $n = 3$ samples. b,c) Microscopy images recorded from the GFP, AF594 and bright field (BF) channels, showing the translation of D2 and D5R-n, respectively. Both samples were transfected with C+L for 24 h; the image width corresponds to 200 μ m. d,e) The uptake pathway of D2 and D5R-n, respectively, was studied using different inhibitors with * denoting significant inhibition ($p < 0.05$). The data is given as avg ± s.d. of $n = 3$ samples, where NA denotes samples without inhibiting agents (uptake set to 100 % and used as a reference level for the samples with inhibitors). f) Microscopy images displaying an overlay of BF and AF594 channels, showing the uptake of D2 transfected with C+L. The image width corresponds to 200 μm.

integration required for D4 folding. Interestingly, changing the helical pitch to 11 bp per turn (D5) helped to overcome any constraints, resulting in the most rigid structure. The combination of a simple scaffold routing, like in D1–D2 and a helical pitch of 11 bp per turn allowed to instantly assemble also longer (≈2–3.5×) mRNA scaffolds into correctly folded mRNA-DNA origami structures. In addition, when comparing D1 and D2, the staple CO spacing seems to have a large influence on the folding yield.

Moreover, the CO spacing has been found to greatly impact the stability of DNA origami structures,[31,53,54] which is in line with our observations. Despite the similar staple CO spacing (42 bp vs 44 bp intervals), D2 was found to be slightly more susceptible to RNase H degradation than D5R-n, most likely caused by the scaffold routing. The lack of the two scaffold COs in the center of the structure may lead to a less compact structure, while simultaneously increasing the flexibility, and by this, the structure becomes more accessible to endonucleases.

The contribution of the helical geometry is reflected in particular upon treatment with DNase I, with D5R-n outperforming D2. Since the activity of DNase I is known to depend on the width of the minor groove,[55] D2 is considered more prone to digestion, assuming that the formed mRNA-DNA double helix indeed adopts a helical pitch of 10.5 bp per turn. Indeed, when comparing the electrophoretic mobility of both variants, sharp bands were observed for D5R-n, while the bands for D2 showed a smearing behavior, suggesting degradation of the DNA staple strands. The degradation could also be monitored in the A647 channel, which tracks the A590 fluorophore. A release of A590 was also observed for D5R-n, which could be attributed to the DNase I degradation of the DNA-DNA duplexes formed between the fluorophore-carrying strand and the core staple overhangs.

In general, packaging the mRNA into the presented origami structures was found to make it more stable compared to its free solution form. However, for its applicability, the mRNA must also be readily translated. The translation efficiency was found to depend on (at least) two factors, which are crucial to consider during the design process. First, the translation needs to be initiated, which is a highly complex process requiring several initiation factors.[42] In brief, a preinitiation complex is formed whose binding to the 5'-end of the mRNA is mediated by cap-binding proteins and an RNA helicase. Due to their interaction with a poly(A)-binding protein, a stable "closed-loop" structure is established.[42] To this end, the 3'-poly(A)-tail and the 5'-cap region should be designed to be placed in close proximity. Subsequently, the untranslated 5'-cap region is being scanned base-by-base by the preinitiation complex for the AUG start codon, which requires mRNA to be present in a single-stranded form, a process assisted by RNA helicases to remove secondary structures. Once recognized, the elongation phase of the protein synthesis can be initiated.[42] Thus, integrating the entire 5'-cap region into the core as in D5 most likely interferes with the binding of the preinitiation complex to the 5'-end, resulting in no observable translation when the variant was subjected to the reticulocyte lysate. A similar behaviour has been observed for structures lacking the 5'-cap.[25]

Secondly, the translation can only proceed given that the assembled structure unfolds, i.e., the mRNA is sequentially "unzipped" from the DNA staples while the ribosome moves toward the 3'-end. Unwinding of helical structures by ribosomal helicases has been reported for both RNA-RNA and RNA-DNA duplexes.[56] Even though both D2 and D5R-n featured a free, single-stranded 5'-cap region and a poly(A)-tail, the translation efficiency of D2 was found to be on average 1.5× higher than that of D5R-n ($P = 0.045$), and when tested in a mammalian cell culture, the difference was even more pronounced ($P = 0.017$, C+L, 24 h). We therefore suggest a dependency between the denaturing process and the internal design including the position of the scaffold crossovers and, more importantly, the presence of free scaffold loops. To this end, D2 possessed free scaffold loops at the end of each helix, aiding to release potential strain at the respective ends of the structure and subsequently promote unfolding. This in return indicates a trade-off in flexibility and compactness of the folded structure between a high translation efficiency and its stability against for instance nucleases. The stability, however, can also be enhanced by complexation with virus capsid proteins.

The accessibility of the 5'-cap region is also essential in cells, which in return requires efficient release of the mRNA-DNA origami from its protective coating after the uptake of the complexes. We observed a significant increase in transfection efficiency for mRNA-DNA origami upon complexation with CCMV capsid proteins, a property of plant viruses previously reported for DNA origami[47] and oligonucleotides.[57,58] The CCMV coating (C) was found to outperform the commercially available transfection agent LP2000. Since the combination C+L showed a similar transfection efficiency, CCMV is suggested to be the driving force for the enhanced uptake.

The uptake of nanoparticles commonly follows the endocytotic pathway, however, it is dependent on the cell line as well as on the shape and chemical composition or the biological origin of the nanoparticle.[59,60] To this end, the uptake can be distinguished between macropinocytosis, clathrin-mediated, and caveolin-mediated endocytosis.[6] Several viruses, including Simian virus 40[61] and cowpea mosaic virus,[62] follow the caveolin-mediated pathway which might be preferential in avoiding lysosomal degradation. In HeLa cells, CCMV is preferentially internalized through the clathrin-mediated endocytosis, though caveolin-mediated endocytosis can occur.[59] The significant inhibition of the uptake of both D2 and D5R-n complexed with C and C+L using dynasore suggests mainly clathrin- and caveolin-dependent endocytosis which is in line with the previous findings. While dynasore also shows an inhibiting effect on L-samples, it was found less pronounced compared to C- or C+L-samples. It should be noted that the uptake was not completely elimited with any inhibitor, suggesting the possibility of multiple pathways.

Recent investigations on the transfection efficiency have demonstrated that not only the mass and the size of the nanoparticle, but also its shape (often referred to as aspect ratio, i.e., the ratio between the long and the short axis of the nanoparticle),[63–66] play a role in uptake. For rod-like DNA origami nanoparticles, an aspect ratio of 1–3 and a length between 50–80 nm were found to be favorable.[63] The presented complexed mRNA-DNA origami variants had, based on the dimensions of the two populations obtained from TEM (Figure 4d), aspect ratios of 1.56 and 2.50 for D2, and 2.25 and 2.84 for D5R-n, and should therefore be efficiently internalized by the cells. Nevertheless, it is notable that for both C- and C+L-samples, D5R-n showed a higher uptake than

D2. This might be attributed to the length of the complexed structures, since locally flat parts at a nanoparticle's surface may facilitate membrane adhesion at low adhesion strengths.[67] Additionally, small differences in the uptake pathway could be observed. The contribution of macropinocytosis for the uptake of both L- and C+L-samples for D5R-n suggests the presence of larger particles or aggregates. Moreover, while filipin III affected D5R-n (C, C+L), no impact was found for D2, suggesting a preference for clathrin-mediated endocytosis for D2-C+L, since neither nystatin inhibited its uptake.

For a nanoparticle taken up through clathrin-mediated endocytosis, the formed vesicle was reported to fuse with an early endosome in HeLa cells.[59] The subsequent release of nucleic acids from the virus capsid shell as well as from the endosome after internalization is, however, not well studied. Although the uptake of especially C- and C+L-origami samples was efficient, the translation into EGFP is low compared to plain mRNA transfected with LP2000. Similarly, the complexation of the plain mRNA with CCMV virus capsid proteins drastically decreased the translation into EGFP (Figure S26a, Supporting Information). A similar behavior of mRNA-loaded virus-like particles has been reported in baby hamster kidney cells (BHK-21), most likely arising from a poor release of mRNA from the CCMV shell.[68]

To further investigate the importance of the disassembly of the capsid shell upon translation, C-samples were incubated with heparin before subjection to reticulocyte lysate. Heparin acts as a negative competing agent, which should therefore trigger the release of mRNA/mRNA-DNA origami from the virus capsid shell (Note S16, Supporting Information). When complexed structures were treated with an excess of heparin before extracellular translation, ≈10 % of the EGFP signal could be recovered for the plain mRNA, but neither D2 nor D5R-n showed any fluorescence, suggesting poor or incomplete release from the capsid coat and a (partially) inaccessible 5'-cap region.

In general, nucleic acids are considered to be released slowly via the small pores of the capsid, however, when they are tightly packed, a more rapid release by rupture is conceivable.[69] LP2000, for one, is suggested to interact with the endosome, resulting in destabilization of the endosomal membrane and subsequent gradual release of the cargo into the cytosol of HeLa cells.[70] By using LP2000 as an additional transfection agent on top of the CCMV coating (C+L), we were able to recover the EGFP signal, indicating the adjuvant's importance for successful endosomal escape. Interestingly, the impact of LP2000 on the size and shape of the capsid coated mRNA-DNA origami (Figure S24b,d, Supporting Information) as well as on its surface properties during the uptake was found minimal. When comparing the inhibitor efficiencies, a significant difference between L- and C+L-samples was detected, which was particularly pronounced for D5R-n, whereas C and C+L followed each other closely, suggesting the virus capsid proteins to be mainly responsible for the enhanced uptake. Our results therefore suggest a synergistic effect between virus capsid proteins and LP2000 for the delivery and translation of mRNA-DNA origami, due to enhancement of transfection while reducing cell toxicity, and greatly promoting endosomal escape, respectively. Once the 5'-cap region is accessible in the cytosol, the mRNA is translated through stepwise "unzipping". While the folding into bundles might partly compromise the translation efficiency of mRNA, the low intensity of the green fluorescence signal arises additionally from the type of delivery vehicle. In comparison to the approaches that complex several mRNA molecules with Lipofectamine into a single particle,[71] it is noteworthy that our multicomponent delivery platform allows control over the number of mRNA molecules, as it encapsulates precisely one mRNA molecule per complex. Also the complex size and shape can be tuned, which in return impacts its uptake.

3. Conclusion

In conclusion, our results provide a first set of design rules for the successful application of mRNA-DNA origami, highlighting the importance of the accessibility of the start codon for translation initiation and simple scaffold routing to achieve successful translation. Utilizing the DNA origami technique in combination with virus capsid proteins allows to program the size and shape of the nanocarrier template, which in return can be used to modulate the cellular uptake. Additionally, the electrostatic-based complexation enables the assembly of other virus species, and therefore, possible exploitation of the virus' innate tropism for delivery. Moreover, precise attachment of cargo molecules onto the mRNA-DNA origami structures as well as functionalization of the virus capsid proteins with targeting molecules or ligands could be used.[72–74] These features could be harnessed in aiding endosomal escape and in achieving highest possible protection and transfection while simultaneously ensuring full release of the mRNA-DNA origami and the accessibility of the start codon. The modularity of the proposed platform would allow for the further development of multipurpose systems for versatile applications in gene delivery and imaging.

4. Experimental Section

Design, Folding and Purification of mRNA-DNA Origami Structures: The design of the 6HB mRNA-DNA origami variants was based on a honeycomb lattice, and their routing was aided using caDNAno.[75] The mRNA-DNA origami variants were then folded isothermally in a one-pot reaction. The 996-nt-long EGFP encoding mRNA scaffold, which, according to the manufacturer is capped at its 5'-end to resemble the naturally occurring Cap-1 structure, was purchased from TriLink Bio Technologies (CleanCap EGFP mRNA, L-7601) and the DNA staple strands were obtained from Integrated DNA Technologies. The annealing reaction was performed in an optimized, variant-specific, buffered environment ("folding buffer," FOB). During the screening, Tris-based as well as HEPES-based buffers were tested, the specific buffer conditions and thermal gradients used are described in Notes S1 and S2 (Supporting Information). For all folding reactions the final concentration of the mRNA was kept constant at 50 nM, and the staple strands (Note S17, Supporting Information) were used in 10× excess (500 nM). Based on the screening, the final FOB containing 1× TAE was supplemented with 5 mM $MgCl_2$ (D1, D2), 2.5 mM $MgCl_2$ (D3, D4), or 5 mM $MgCl_2$ and 1 mM NaCl (D5 variants). The mRNA and staples strands were mixed and annealed in a 15 min incubation at 55 °C, followed by a 10 min incubation on ice before storage at 4 °C. The folding conditions for FLuc and β-gal are described in Note S6 (Supporting Information).

Spin-filtration was used to remove excess staple strands after the annealing. Briefly, 400 µL of 1× FOB were added to the spin-filter (100 kDa molecular weight cut-off, MWCO, Amicon) for washing purposes and centrifuged at 14 000 g for 5 min. Subsequently, the reaction mixture and the 1× FOB were added in 1:1 ratio twice, first 40 µL, followed by

30 µL, and centrifuged at 6000 g for 10 min. Then, the structures were washed 3× with 80 µL of 1× FOB and twice with 80 µL RNase-free water (6000 g, 10 min). By inverting the filter into a clean tube (1000 g, 2.5 min), the sample was recovered. The concentration of the purified structure was determined from an absorbance measurement at 260 nm using Lambert–Beer's Law (Note S18, Supporting Information).

Agarose Gel Electrophoresis: Agarose gel electrophoresis was used to monitor the folding of the mRNA-DNA origami as well as the removal of unbound staple strands after purification. To this end, a 3.5 % (w/v) agarose gel (1× TAE buffer, 11 mM $MgCl_2$) was run at 90 V for 45 min in running buffer containing 1× TAE and 11 mM $MgCl_2$. This technique was furthermore used to observe the binding interaction between the nucleic acids and the virus capsid proteins as well as to study the intactness of the structures upon nuclease treatment, however, the agarose concentration was decreased to 2 % (w/v). All samples were mixed with 40 % (w/v) sucrose (1:5) or 6× gel loading dye (for samples not containing A590), and EtBr (final concentration 0.46 µg mL^{-1}) was used for staining. The nucleic acids were imaged under both ultraviolet light (EtBr) and, if applicible, red light (A647 channel) using a ChemiDoc MP system (Bio-Rad).

Capsid Protein Coating of mRNA-DNA Origami: The complexation of mRNA-DNA origami with CCMV capsid proteins was performed according to ref. [46] Briefly, CCMV particles were dialysed overnight in Slize-A-Lyzer Mini Dialysis cups (3.5 kDa MWCO, Thermo Scientific) against 50 mM Tris-HCl buffer, pH 7.5 supplemented with 500 mM $CaCl_2$ and 1 mM dithiothreitol (DTT), followed by a 6 h centrifugation step (21 000 g, 4 °C) to pellet the RNA. The supernatant containing the capsid proteins was subjected to another overnight dialysis against "clean buffer" (50 mM Tris, pH 7.5 supplemented with 150 mM NaCl and 1 mM DTT). To determine the concentration of the isolated capsid proteins, the absorbance at 280 nm was measured (extinction coefficient 23 590 M^{-1} cm^{-1}) on a BioTek Eon Microplate Spectrophotometer using a Take3 plate (2 µL sample).

Subsequently, the virus capsid proteins were mixed with purified mRNA-DNA origami in 1× FOB in 1:1 ratio resulting in a complexation buffer containing 45 mM Tris, 75.5 mM NaCl, 10 mM acetic acid, 2.5 mM $MgCl_2$, 0.5 mM DTT and 0.5 mM EDTA, and incubated for at least 1 h at 4 °C. For the evaluation of the coating by AGE and TEM, the final origami concentration after complexation was 7.5 nM, for the enzymatic stability studies, complexation was performed at 10 nM and for the mammalian cell culture assay 31 nM were used.

Enzymatic Stability Studies: The stability of plain mRNA, as well as plain and complexed mRNA-DNA origami structures in nuclease-rich environment was evaluated using RNase A (from bovine pancreas, Sigma Aldrich, 10109169001), RNase H (NEB, M0297S) and DNase I (from bovine pancreas, Sigma Aldrich, D4263). To this end, 2 µL of the enzyme stock (range 0–500 U mL^{-1}) were added to 15 µL of the sample solution. The final buffer contained 33.75 mM Tris, 7.5 mM acetic acid, 0.375 mM DTT, 0.375 mM EDTA, and after the salt concentration (3 µL, NaCl, $CaCl_2$, and $MgCl_2$) was adjusted for each sample to ensure optimal conditions for the enzyme, the resulting final sample concentration is 7.5 nM (20 µL). For samples containing plain mRNA, 22.5 nM were chosen as final sample concentrations for easier detection. For both RNase H and DNase I, the NaCl concentration was kept constant at 56.6 mM. Nevertheless, the $MgCl_2$ salt concentration was increased to 10 mM for RNase H, and to 5 mM for DNase I. The DNase I buffer was additionally supplemented with 1 mM $CaCl_2$. Incubation with RNase A was performed by increasing the NaCl concentration to 500 mM. All enzymes were incubated with the sample at 37 °C for 20 min, after which the sample was placed on ice, mixed with 40 % sucrose (4 µL) and loaded on a 2 % (w/v) agarose gel. Analysis of the band intensities and R_f for RNase A was performed with ImageJ and Origin. R_f was determined as $\frac{r-r_0}{r_0}$, where r is the measured distance between the leading band of the treated sample and the gel pocket, while r_0 is the migration distance obtained for the untreated origami sample.

Translation Studies Using Reticulocyte Lysate: The capability of different mRNA-DNA origami structure variants to translate into EGFP was studied using a Retic Lysate IVT Kit (Thermo Scientific), following the manufacturer's instructions with slight modifications. Briefly, 17 µL of reticulocyte lysate (obtained from rabbits) were supplemented with 1 µL amino acid mix (methionine, leucine at concentrations of 1.25 mM), 1.25 µL 20× translation mix (1.6 M CH_3CO_2K, 10 mM $Mg(CH_3COO)2$, 200 mM creatine phosphate and 0.5 mM of both methonine and leucine) and 0.25 µL nuclease-free water. Finally, 5 µL of nucleic acid template were added, resulting in total nucleic acid content of 50 ng for mRNA-DNA origami variants or 5–12 ng for plain mRNA. For reactions studying the strand-displacement, D5R-6 and D5R-10 were incubated for 10 min with 10× excess of invader strands. The samples were vortexed gently followed by brief centrifugation before incubating them for 2 h in a 30 °C waterbath. To digest tRNAs in the reaction mixture, 2.5 µL of 1 mg mL^{-1} RNase A (Sigma Aldrich, 10109169001) were added for 10 min, after which the reaction was stopped by placing the tubes on ice for at least 5 min. The samples were finally stored at −20 °C.

The outcome of the reaction was analysed using native PAGE (4-20% Mini-PROTEAN TGX Precast Protein Gels, Bio-Rad, 4561096). 1 µL of the retic lysate reaction was diluted with 2 µL 1× PBS and mixed with 2× sample buffer containing 62.5 mM Tris, 40 % (v/v) glycerol and 0.01 % (w/v) bromophenol blue. The gel was run in 25 mM Tris buffer pH 8.3 supplemented with 192 mM glycine at 200 V for 40 min on ice. EGFP was visualized under blue light (A488 channel) with a ChemiDoc MP system (Bio-Rad). The fluorescence intensities were analysed using ImageJ and Origin, the significance was calculated from averaged triplicate samples with a heteroscedastic *t*-test with a two-tailed distribution.

Mammalian Cell Culture Studies: For the cell culture studies, the HeLa cell line was used. It was maintained in complete media consisting of high glucose Dulbecco's Modified Eagle's Medium (DMEM, Sigma-Aldrich) supplemented with 5 % fetal bovine serum (FBS, Gibco). Penicillin and streptomycine (final concentrations 100 U mL^{-1} and 100 µg mL^{-1}, respectively, Gibco) were added to prevent bacterial contamination. The cells were grown in petridishes (Corning) in a humidified 5 % CO_2 atmosphere at 37 °C. Once the cells reached a confluency of 90 %, they were passaged by incubation with 0.5 % Trypsin-EDTA solution (Sigma-Aldrich) for 5 min to facilitate detachment.

In order to study transfection, the cells (5000 cells/well) were seeded on 96-well plate (black/clear bottom, TC treated surface, Thermo Scientific) and incubated for 24 h. Prior to transfection, the cells were washed with 1× PBS. Then, the samples were transfected for 16 or 24 h in Opti-MEM (Thermo Fisher). To allocate sufficient time for the decomplexation of the samples, Opti-MEM was replaced with complete media and the cells were grown for additional 24 h (16 h transfection) or over night (24 h transfection). For analysis, the wells were first washed with 100 µL 1× PBS to remove residues of the complete media, and then measured in 100 µL 1× PBS.

All samples (N, L, C and C+L) were in a first step either complexed with virus capsid proteins (250× excess), resulting in a mRNA-DNA origami concentration of 31 nM, or diluted into complexation buffer, matching the concentration. Subsequently, the samples were diluted 1:1 into Opti-MEM, which, for samples treated with Lipofectamine 2000 (Invitrogen) contained 2 % (v/v) (0.7 µL) of the transfection agent, at a minimum of 5 min before addition of 20 µL per well, corresponding to 100 ng of RNA.

The success of the transfection was evaluated by measuring the fluorescence emission of both EGFP (520 nm) and A590 (616 nm) in a microplate reader (Cytation 3, BioTek), using excitation wavelengths of 490 nm and 584 nm, respectively. For visualization, the samples were imaged at 20× magnification in bright field (BF) and with EGFP (470 nm) and AF594 (590 nm) filter sets using a Zeiss Axio Observer Z1 microscope. The exposure times for the fluorescence channels was set to 300 ns, and the intensity to 70 % (EGFP) and 65 % (AF594), with exception of plain mRNA samples treated with LP2000 (75 ns exposure, 25 % intensity).

For data treatment, the data from triplicate samples was averaged and normalized by subtracting 90 % or 50 % of the background signal from the buffer for EGFP and A590, respectively. For EGFP the intensities of the coated samples were plotted relative to the respective naked mRNA-DNA origami. The significance was calculated with a *t*-test with a two-tailed distribution.

The uptake studies have been performed as previously reported.[59] In short, 5000 cells/well were seeded on a 96-well plate (black/clear bottom, TC treated surface, Thermo Scientific) and grown for 24 h. Subsequently, the cells were washed with 1× PBS, after which the media was replaced with 80 µL of inhibitor-supplemented Opti-MEM for 30 min pre-treatment of the cells. To this end, sucrose was diluted to 225 mM, cytochalasin D to 4 µ M, chlorpromazine to 10 µ M, filipin III to 3 µ M, nystation to 20 µ M, and dynasore to 100 µ M. Then, the samples (complexed with either L, C or C+L) were diluted into fresh opti-MEM, in which the inhibitor concentration had been adjusted, resulting in a sample concentration of 15.6 nM. 20 µL were added per well, corresponding to 100 ng of mRNA, and incubated for 4 h, followed by a washing step with 1× PBS. The inhibition of the uptake was evaluated based on the A590 signal, and the readout and imaging were performed as for the transfection studies in 100 µL 1× PBS.

Atomic Force Microscopy: A 20 µL droplet of 10 nM origami solution diluted in 1× TAE buffer supplemented with 12.5 mM $MgCl_2$ was deposited onto a freshly cleaved mica substrate (Electron Microscopy Sciences). The sample was incubated for 1 min, after which it was washed three times with 100 µL RNase-free water which was blotted away immediately. A steady nitrogen stream was used to dry the sample, after which it was immediately imaged. The measurements were performed in air using ScanAsyst Air mode in combination with ScanAsyst-Air probes (Bruker) on a Dimension Icon AFM (Bruker). The AFM images were processed in NanoScope Analysis v. 1.90, and for easier comparison the height scale was adjusted.

Transmission Electron Microscopy: Both plain mRNA-DNA origami as well as samples complexed with capsid proteins were prepared at a concentration of 7.5 nM, while for complexed mRNA samples 22.5 nM were used. After depositing a sample-containing droplet (3 µL) for 3 min on a plasma cleaned (15 s oxygen plasma flash, NanoClean 1070, Fishione Instruments) Formvar carbon-coated copper grid (FCF400Cu, Electron Microscopy Sciences), the droplet was removed by blotting against filter paper. Subsequently, the grid was negative stained in a two-step procedure using an aqueous 2 % (w/v) uranyl formate solution[28] which had been supplemented with 25 mM NaOH to adjust the pH. After immersing the grid in a 5 µL stain droplet and immediate blotting, the grid was immersed into a 20 µL stain droplet. A final blotting step was performed after 45 s, after which the grids were dried for at least 15 min. The imaging was performed either at an acceleration voltage of 100 kV on a JEOL JEM-2800 electron microscope or at 120 kV on a FEI Tecnai 12 Bio-Twin microscope.

Cryo-EM Data Collection and Analysis: For cryo-EM, 3 µL of 100 nM D5 in 1× FOB were deposited on a plasma-cleaned (50 s, Harrick Plasma PDC-002-EC instrument) holey carbon-coated grid (copper 200 mesh R1.2/1.3, Quantifoil). Using a vitrification apparatus (Vitrobot, Thermo Fisher Scientific), excess liquid was blotted away immediately for 2 s at 100 % relative humidity and 6 °C. Subsequently, the grid was plunged in liquid ethane and stored in liquid nitrogen. Initial screening was performed on a 200 kV Talos Arctica microscope, equipped with a Falcon 4i detector and an energy filter set at 20 eV. Data were collected at a pixel size of 0.922 Å px^{-1} and the electron dose used was 50.8 e^{-} $Å^{-2}$. Large scale EM data collection was performed on a 300 kV Titan Krios microscope, equipped with a Gatan K3 direct electron detector and an energy filter at 20 eV. Data were collected at a nominal pixel size of 0.825 Å px^{-1}. The used electron dose was 42.6 e^{-} $Å^{-2}$, fractionated to 40 frames over 2 s exposure time. A total of 13 416 movies were collected.

Data were processed using cryoSPARC (v.4.6).[76] The movie frames were aligned using patch motion correction and CTF parameters estimated using patch CTF estimation. The micrographs were curated manually to a set of 12 974 micrographs. Initial particle picking and processing were performed using blob picker on a subset of the total micrographs (1008), then well-aligning 1-helix particles (9537) were identified using 2D classification. The resulting 2D class averages were used as templates for template-based picking from a subset of micrographs (4324). The particles were further classified in 2D, and a subset of 2-helix class averages was identified and a subset of the particles (1456 of 5915) in the micrographs containing the highest number of particles were used to train a TOPAZ model.[77] The model was used to pick particles from the entire set of curated micrographs. Extensive 2D classification of the resulting particles (6 levels) resulted in a set of particles corresponding to 37 831 side-views of the 3-helix bundles. Final 2D classification was performed on particles extracted at 784 px, Fourier cropped to 392 px, without masking, using a batch size of 200 and a maximum resolution of 15 Å.

Molecular Simulations: To perform coarse-grained molecular dynamic simulations, the caDNAno origami design file was first converted to an oxDNA format using tacoxDNA.[78] The oxDNA simulation were run with the oxNA model to simulate RNA-DNA hybrids.[79] The structure was then relaxed in two steps (Monte Carlo and molecular dynamics relaxation) to remove local stresses, e.g. overlapping nucleotides. Subsequently, the structure was simulated for 1× 10^8 steps, with a time step corresponding to 0.005 oxDNA time units. For the simulations, a salt concentration of 0.5 M and a temperature of 30 °C with a 'john' thermostat emulating Brownian dynamics were used, and a configuration was saved every 2× 10^4 steps. The mean structure, the distances and the RMSF values were calculated using the oxDNA analysis tool.[40] The RMSF values were visualized using oxView.[40,41]

Statistical Analysis: Statistical analysis was performed to determine the average dimension of plain and complexed mRNA-DNA origami structures obtained from TEM. The dimensions are given as (average (avg) ± s.d.) throughout and the sample size is stated alongside. For detailed data treatment and statistical analysis performed for 'translation studies using reticulocyte lysate' as well as 'mammalian cell culture studies' the reader is referred to the corresponding experimental section. In general, these experiments were performed as triplicates.

Supporting Information

Supporting Information is available from the Wiley Online Library or from the author.

Acknowledgements

The authors acknowledge financial support from the European Research Council (ERC) and ERA Chair MATTER under European Union's Horizon 2020 research and innovation programme (grant agreement no. 101002258 and 856705), Academy of Finland (project no. 341908), Emil Aaltonen Foundation and Jane and Aatos Erkko Foundation. The authors thank Ahmed Shaukat for his assistance with cell culturing. This work was carried out under the Academy of Finland Centers of Excellence Program (2022-2029) in Life-Inspired Hybrid Materials (LIBER), project number (346110). The authors acknowledge the provision of facilities and technical support by Aalto University Bioeconomy Facilities, OtaNanoNanomicroscopy Center (Aalto-NMC) and Micronova Nanofabrication Center. We thank Kiran Ahmad and Tuomas Niemi-Aro (University of Helsinki) for technical assistance in cryoEM. The facilities and expertise of the HiLIFE CryoEM unit at the University of Helsinki, a member of Instruct-ERIC Centre Finland, FINStruct, and Biocenter Finland are gratefully acknowledged. For SciLifeLab (Stockholm), we thank Karin Walldén for data collection support.

Open access publishing facilitated by Aalto-yliopisto, as part of the Wiley - FinELib agreement.

Conflict of Interest

The authors declare no competing interests.

Author Contributions

I.S., S.S., and M.A.K. conceptualized the project, while I.S. and V.L. designed the origami structures. Characterization was performed by I.S. and S.S., and translation using reticulocyte lysate was conducted by I.S. Mammalian cell studies were carried out by J.W., S.S., and I.S. Cryo-EM and particle averaging were performed by E.-P.K. and J.T.H., while molecular simulations were conducted by I.S. and B.S. CCMV production was handled by J.J.L.M.C. The manuscript was written by I.S., V.L., and M.A.K., with inputs from all authors.

Data Availability Statement

The data that support the findings of this study are available from the corresponding author upon reasonable request.

Keywords

cellular delivery, mRNA-DNA origami, mRNA translation, virus capsid proteins

Received: November 14, 2024
Revised: January 28, 2025
Published online: February 27, 2025

[1] J. A. Kulkarni, D. Witzigmann, S. B. Thomson, S. Chen, B. R. Leavitt, P. R. Cullis, R. van der Meel, *Nat. Nanotechnol.* **2021**, *16*, 630.
[2] W. Zhao, X. Hou, O. G. Vick, Y. Dong, *Biomater.* **2019**, *217*, 119291.
[3] H. Lee, A. K. R. Lytton-Jean, Y. Chen, K. T. Love, A. I. Park, E. D. Karagiannis, A. Sehgal, W. Querbes, C. S. Zurenko, M. Jayaraman, C. G. Peng, K. Charisse, A. Borodovsky, M. Manoharan, J. S. Donahoe, J. Truelove, M. Nahrendorf, R. Langer, D. G. Anderson, *Nat. Nanotechnol.* **2012**, *7*, 389.
[4] U. Sahin, A. Muik, E. Derhovanessian, I. Vogler, L. M. Kranz, M. Vormehr, A. Baum, K. Pascal, J. Quandt, D. Maurus, S. Brachtendorf, V. Lörks, J. Sikorski, R. Hilker, D. Becker, A.-K. Eller, J. Grützner, C. Boesler, C. Rosenbaum, M.-C. Kühnle, U. Luxemburger, A. Kemmer-Brück, D. Langer, M. Bexon, S. Bolte, K. Karikó, T. Palanche, B. Fischer, A. Schultz, P.-Y. Shi, et al., *Nature* **2020**, *586*, 594.
[5] E. J. Anderson, N. G. Rouphael, A. T. Widge, L. A. Jackson, P. C. Roberts, M. Makhene, J. D. Chappell, M. R. Denison, L. J. Stevens, A. J. Pruijssers, A. B. McDermott, B. Flach, B. C. Lin, N. A. Doria-Rose, S. O'Dell, S. D. Schmidt, K. S. Corbett, P. A. Swanson II, M. Padilla, K. M. Neuzil, H. Bennett, B. Leav, M. Makowski, J. Albert, K. Cross, V. V. Edara, K. Floyd, M. S. Suthar, D. R. Martinez, R. Baric, et al., *N. Engl. J. Med.* **2020**, *383*, 2427.
[6] S. Behzadi, V. Serpooshan, W. Tao, M. A. Hamaly, M. Y. Alkawareek, E. C. Dreaden, D. Brown, A. M. Alkilany, O. C. Farokhzad, M. Mahmoudi, *Chem. Soc. Rev.* **2017**, *46*, 4218.
[7] R. Singh, P. Yadav, H. A. Naveena, D. Bhatia, *Nanoscale* **2023**, *15*, 1099.
[8] Y.-j. Jung, J. S. Choi, J.-y. Ryu, Z. Zhang, Y.-b. Lim, *J. Am. Chem. Soc.* **2023**, *145*, 23048.
[9] P. W. K. Rothemund, *Nature* **2006**, *440*, 297.
[10] H. Dietz, S. M. Douglas, W. M. Shih, *Science* **2009**, *325*, 725.
[11] S. M. Douglas, H. Dietz, T. Liedl, B. Högberg, F. Graf, W. M. Shih, *Nature* **2009**, *459*, 414.
[12] S. Dey, C. Fan, K. V. Gothelf, J. Li, C. Lin, L. Liu, N. Liu, M. A. D. Nijenhuis, B. Saccà, F. C. Simmel, H. Yan, P. Zhan, *Nat. Rev. Methods Primers* **2021**, *1*, 13.
[13] G. A. Knappe, E.-C. Wamhoff, M. Bathe, *Nat. Rev. Mater.* **2023**, *8*, 123.
[14] J. Weiden, M. M. C. Bastings, *Curr. Opin. Colloid Interface Sci.* **2021**, *52*, 101411.
[15] Q. Jiang, Y. Shang, Y. Xie, B. Ding, *Adv. Mater.* **2023**, 2301035.
[16] F. A. S. Engelhardt, F. Praetorius, C. H. Wachauf, G. Brüggenthies, F. Kohler, B. Kick, K. L. Kadletz, P. N. Pham, K. L. Behler, T. Gerling, H. Dietz, *ACS Nano* **2019**, *13*, 5015.
[17] J. A. Kretzmann, A. Liedl, A. Monferrer, V. Mykhailiuk, S. Beerkens, H. Dietz, *Nat. Commun.* **2023**, *14*, 1017.
[18] A. Liedl, J. Grießing, J. A. Kretzmann, H. Dietz, *J. Am. Chem. Soc.* **2023**, *145*, 4946.
[19] U. Sahin, K. Karikó, Ö. Türeci, *Nat. Rev. Drug Discovery* **2014**, *13*, 759.
[20] M. Hu, C. Feng, Q. Yuan, C. Liu, B. Ge, F. Sun, X. Zhu, *Nat. Commun.* **2023**, *14*, 1307.
[21] C. Geary, P. W. K. Rothemund, E. S. Andersen, *Science* **2014**, *345*, 799.
[22] C. Geary, G. Grossi, E. K. S. McRae, P. W. K. Rothemund, E. S. Andersen, *Nat. Chem.* **2021**, *13*, 549.
[23] E. K. S. McRae, H. Ø. Rasmussen, J. Liu, A. Bøggild, M. T. A. Nguyen, N. S. Vallina, T. Boesen, J. S. Pedersen, G. Ren, C. Geary, E. S. Andersen, *Nat. Nanotechnol.* **2023**, *18*, 808.
[24] M. Endo, S. Yamamoto, K. Tatsumi, T. Emura, K. Hidaka, H. Sugiyama, *Chem. Commun.* **2013**, *49*, 2879.
[25] X. Wu, Q. Liu, F. Liu, T. Wu, Y. Shang, J. Liu, B. Ding, *Nanoscale* **2021**, *13*, 12848.
[26] L. Zhou, A. R. Chandrasekaran, M. Yan, V. A. Valsangkar, J. I. Feldblyum, J. Sheng, K. Halvorsen, *Nanoscale Adv.* **2021**, *3*, 4048.
[27] M. F. Parsons, M. F. Allan, S. Li, T. R. Shepherd, S. Ratanalert, K. Zhang, K. M. Pullen, W. Chiu, S. Rouskin, M. Bathe, *Nat. Commun.* **2023**, *14*, 382.
[28] C. E. Castro, F. Kilchherr, D.-N. Kim, E. L. Shiao, T. Wauer, P. Wortmann, M. Bathe, H. Dietz, *Nat. Methods* **2011**, *8*, 221.
[29] E. Torelli, B. Shirt-Ediss, S. A. Navarro, M. Manzano, P. Vizzini, N. Krasnogor, *Int. J. Mol. Sci.* **2023**, *24*, 8483.
[30] N. C. Horton, B. C. Finzel, *J. Mol. Biol.* **1996**, *264*, 521.
[31] Y. Xin, P. Piskunen, A. Suma, C. Li, H. Ijäs, S. Ojasalo, I. Seitz, M. A. Kostiainen, G. Grundmeier, V. Linko, A. Keller, *Small* **2022**, *18*, 2107393.
[32] M. G. AbouHaidar, I. G. Ivanov, *Zeitschrift für Naturforschung C* **1999**, *54*, 542.
[33] Y. Li, R. R. Breaker, *J. Am. Chem. Soc.* **1999**, *121*, 5364.
[34] N. M. Fischer, M. D. Polêto, J. Steuer, D. van der Spoel, *Nucleic Acids Res.* **2018**, *46*, 4872.
[35] R. Shiman, D. E. Draper, *J. Mol. Biol.* **2000**, *302*, 79.
[36] R. Guth-Metzler, A. M. Mohamed, E. T. Cowan, A. Henning, C. Ito, M. Frenkel-Pinter, R. M. Wartell, J. B. Glass, L. D. Williams, *Nucleic Acids Res.* **2023**, *51*, 3529.
[37] R. Yamagami, J. L. Bingaman, E. A. Frankel, P. C. Bevilacqua, *Nat. Commun.* **2018**, *9*, 2149.
[38] R. Yamagami, J. P. Sieg, P. C. Bevilacqua, *Biochemistry* **2021**, *60*, 2374.
[39] K. Struhl, in *Curr. Protoc. Mol. Biol., 3.13.1*, (Eds.: F. Ausubel, R. Brent, R. Kingston, D. Moore, J. Seidman, J. Smith, K. Struhl), John Wiley & Sons, Inc, Brooklyn, New York **2003**.
[40] E. Poppleton, J. Bohlin, M. Matthies, S. Sharma, F. Zhang, P. Šulc, *Nucleic Acids Res.* **2020**, *48*, e72.
[41] J. Bohlin, M. Matthies, E. Poppleton, J. Procyk, A. Mallya, H. Yan, P. Šulc, *Nat. Protoc.* **2022**, *17*, 1762.
[42] A. G. Hinnebusch, J. R. Lorsch, *Cold Spring Harbor Perspect. Biol.* **2012**, *4*, a011544.
[43] A. R. Chandrasekaran, *Nat. Rev. Chem.* **2021**, *5*, 225.
[44] A. Naskalska, J. G. Heddle, *Nanomedicine* **2024**, *19*, 1103.
[45] M. Hori, A. Steinauer, S. Tetter, J. Hälg, E.-M. Manz, D. Hilvert, *Nat. Commun.* **2024**, *15*, 3576.
[46] I. Seitz, S. Saarinen, E.-P. Kumpula, D. McNeale, E. Anaya-Plaza, V. Lampinen, V. P. Hytönen, F. Sainsbury, J. J. L. M. Cornelissen, V. Linko, J. T. Huiskonen, M. A. Kostiainen, *Nat. Nanotechnol.* **2023**, *18*, 1205.
[47] J. Mikkilä, A.-P. Eskelinen, E. H. Niemelä, V. Linko, M. J. Frilander, P. Törmä, M. A. Kostiainen, *Nano Lett.* **2014**, *14*, 2196.
[48] T. Tadokoro, S. Kanaya, *The FEBS J.* **2009**, *276*, 1482.
[49] D. H. Sutton, G. L. Conn, T. Brown, A. N. Lane, *Biochem. J.* **1997**, *321*, 481.
[50] D. Dutta, J. G. Donaldson, *Cell. Logist.* **2012**, *2*, 203.
[51] R. Kosinski, A. Mukhortava, W. Pfeifer, A. Candelli, P. Rauch, B. Saccà, *Nat. Commun.* **2019**, *10*, 1061.
[52] M. DeLuca, D. Duke, T. Ye, M. G. Poirier, Y. Ke, C. Castro, G. Arya, *Nat. Commun.* **2024**, *15*, 3015.

[53] A. R. Chandrasekaran, J. Vilcapoma, P. Dey, S. W. Wong-Deyrup, B. K. Dey, K. Halvorsen, *J. Am. Chem. Soc.* **2020**, *142*, 6814.
[54] Z. Ma, K. Kawai, Y. Hirai, T. Tsuchiya, O. Tabata, *Jpn. J. Appl. Phys.* **2017**, *56*, 06GJ02.
[55] D. Suck, A. Lahm, C. Oefner, *Nature* **1988**, *332*, 464.
[56] S. Takyar, R. P. Hickerson, H. F. Noller, *Cell* **2005**, *120*, 49.
[57] C. Pretto, J. C. M. van Hest, *Bioconjugate Chem.* **2019**, *30*, 3069.
[58] H. Cai, S. Shukla, N. F. Steinmetz, *Adv. Funct. Mater.* **2020**, *30*, 1908743.
[59] M. V. de Ruiter, R. M. van der Hee, A. J. M. Driessen, E. D. Keurhorst, M. Hamid, J. J. L. M. Cornelissen, *J. Controlled Release* **2019**, *307*, 342.
[60] X. Liu, F. Wu, Y. Tian, M. Wu, Q. Zhou, S. Jiang, Z. Niu, *Sci. Rep.* **2016**, *6*, 24567.
[61] L. Pelkmans, J. Kartenbeck, A. Helenius, *Nat. Cell Biol.* **2001**, *3*, 473.
[62] E. M. Plummer, M. Manchester, *Mol. Pharmaceutics* **2013**, *10*, 26.
[63] M. M. C. Bastings, F. M. Anastassacos, N. Ponnuswamy, F. G. Leifer, G. Cuneo, C. Lin, D. E. Ingber, J. H. Ryu, W. M. Shih, *Nano Lett.* **2018**, *18*, 3557.
[64] P. Wang, M. A. Rahman, Z. Zhao, K. Weiss, C. Zhang, Z. Chen, S. J. Hurwitz, Z. G. Chen, D. M. Shin, Y. Ke, *J. Am. Chem. Soc.* **2018**, *140*, 2478.
[65] S. Shukla, F. J. Eber, A. S. Nagarajan, N. A. DiFranco, N. Schmidt, A. M. Wen, S. Eiben, R. M. Twyman, C. Wege, N. F. Steinmetz, *Adv. Healthcare Mater.* **2015**, *4*, 874.
[66] A. Rajwar, S. R. Shetty, P. Vaswani, V. Morya, A. Barai, S. Sen, M. Sonawane, D. Bhatia, *ACS Nano* **2022**, *16*, 10496.
[67] S. Dasgupta, T. Auth, G. Gompper, *Nano Lett.* **2014**, *14*, 687.
[68] O. Azizgolshani, R. F. Garmann, R. Cadena-Nava, C. M. Knobler, W. M. Gelbart, *Virology* **2013**, *441*, 12.
[69] L. Sukeník, L. Mukhamedova, M. Procházková, K. Škubník, P. Plevka, R. Vácha, *ACS Nano* **2021**, *15*, 19233.
[70] Z. ur Rehman, D. Hoekstra, I. S. Zuhorn, *ACS Nano* **2013**, *7*, 3767.
[71] C. Leonhardt, G. Schwake, T. R. Stögbauer, S. Rappl, J.-T. Kuhr, T. S. Ligon, J. O. Rädler, *Nanomed.: Nanotechnol. Biol. Med.* **2014**, *10*, 679.
[72] D. Bhatia, S. Arumugam, M. Nasilowski, H. Joshi, C. Wunder, V. Chambon, V. Prakash, C. Grazon, B. Nadal, P. K. Maiti, L. Johannes, B. Dubertret, Y. Krishnan, *Nat. Nanotechnol.* **2016**, *11*, 1112.
[73] A. Krissanaprasit, C. Key, M. Fergione, K. Froehlich, S. Pontula, M. Hart, P. Carriel, J. Kjems, E. S. Andersen, T. H. LaBean, *Adv. Mater.* **2019**, *31*, 1808262.
[74] I. Stupka, Y. Azuma, A. P. Biela, M. Imamura, S. Scheuring, E. Pyza, O. Woźnicka, D. P. Maskell, J. G. Heddle, *Science Advances* **2022**, *8*, eabj9424.
[75] S. M. Douglas, A. H. Marblestone, S. Teerapittayanon, A. Vazquez, G. M. Church, W. M. Shih, *Nucleic Acids Res.* **2009**, *37*, 5001.
[76] A. Punjani, J. L. Rubinstein, D. J. Fleet, M. A. Brubaker, *Nat. Methods* **2017**, *14*, 290.
[77] T. Bepler, A. Morin, M. Rapp, J. Brasch, L. Shapiro, A. J. Noble, B. Berger, *Nat. Methods* **2019**, *16*, 1153.
[78] A. Suma, E. Poppleton, M. Matthies, P. Šulc, F. Romano, A. A. Louis, J. P. Doye, C. Micheletti, L. Rovigatti, *J. Comput. Chem.* **2019**, *40*, 2586.
[79] E. J. Ratajczyk, P. Šulc, A. J. Turberfield, J. P. Doye, A. A. Louis, *The Journal of Chemical Physics* **2024**, *160*, 115101.